Dalton Transactions

Accepted Manuscript

ROYAL SOCIETY OF CHEMISTRY

www.rsc.org/dalton

Journal Name

RSCPublishing

ARTICLE

Hydrothermal Synthesis of Core-shell Structured $TbPO_4:Ce^{3+}$@$TbPO_4:Gd^{3+}$ Nanocomposites for Magnetic Resonance and Optical Imaging

Cite this: DOI: 10.1039/xoxxoooooox

Received ooth January 2012,
Accepted ooth January 2012

DOI: 10.1039/xoxxoooooox

www.rsc.org/

Xiao-yan Kuang[1], Huan Liu[1], Wen-yong Hu[1] and Yuan-zhi Shao[1,2]*

1.School of Physics and Engineering, Sun Yat-sen University, Guangzhou, 510275, China.
2. Sino-French Institute of Nuclear Engineering and Technology, Zhuhai Campus of Sun Yat-sen Univeristy, Zhuhai 519082, China.
* Author to whom all correspondence should be addressed, Email: stssyz@mail.sysu.edu.cn

Multi-modal imaging based on multifunctional nanoparticles provides deep, non-invasive and highly sensitive imaging and is a promising alternative approach that can improve the sensitivity of early cancer diagnosis. In this study, two nanoparticles, $TbPO_4:Ce^{3+}$ and $TbPO_4:Ce^{3+}$@$TbPO_4:Gd^{3+}$, were synthesized via the citric-acid-mediated hydrothermal route, and then systematically characterized by means of microstructure, photoluminescence, magnetic resonance imaging (MRI), biocompatibility, and bioimaging. The results of energy dispersive X-ray spectroscopy (EDS) and electron energy loss spectroscopy (EELS) line scans indicated that $TbPO_4:Gd^{3+}$ nanoshells about 5nm in thickness were successfully coated on the $TbPO_4:Ce^{3+}$ nanocores. X-ray diffraction (XRD) and Fourier transform of high-resolution transmission electron microscope (TEM) images indicated that the core–shell nanocomposites had a single crystal structure. The photoluminescence of the $TbPO_4:Ce^{3+}$ @$TbPO_4:Gd^{3+}$ and $TbPO_4:Ce^{3+}$ nanoparticles was greatly intensified by 200 times and 100 times, respectively, compared with pure $TbPO_4$ nanoparticles. *In vitro* cytotoxicity tests based on the methyl thiazolyl tetrazolium (MTT) assay demonstrated that the monodispersed nanoparticles of $TbPO_4:Ce^{3+}$@$TbPO_4:Gd^{3+}$ had low toxicity. The intracellular luminescence of the nanoparticles after being internalized by HeLa cells was also observed using confocal fluorescence microscopes. MRI showed that the nanoshells of Gd-doped $TbPO_4$ possessed a longitudinal relaxivity of 4.067 $s^{-1}mM^{-1}$, which is comparable to that of the commercial MRI contrast Gd-TDPA. As a result, the core-shell structured $TbPO_4:Ce^{3+}$@ $TbPO_4:Gd^{3+}$ nanoparticles can potentially serve as multifunctional nanoprobes forboth optical biolabels and MRI contrast agents.

Introduction

Early diagnosis is vital for the treatment and prognosis of cancer. Medical imaging technologies usually play an important role in early cancer diagnosis. Existing imaging technologies include magnetic resonance imaging (MRI) [1-4], positron emission tomography (PET) [5-6], optical molecular imaging[7-9], and x-ray computed tomography (CT) [10-12]. Each of these imaging techniques has its advantages and disadvantages. MRI is well-known for its secure, multi-azimuth, high spatial resolution, which is largely unaffected by tissue depth. However, the low sensitivity of MRI limits its application to some extent. Optical molecular imaging based on fluorescence and bioluminescence is highly sensitive and noninvasive, but is currently limited by the low spatial resolution of the imaging and limited detecting depth (1-2 cm) [11]. All existing single modal imaging methods have certain limitations for medical application. Accordingly, it is of both academic and practical value to study the advantages of using different imaging techniques while offsetting their limitations. Owing to their high resolution and large detecting depth in biological tissue, magnetic-optical bimodal nanoparticles have attracted considerable attention in the field of medical diagnosis and molecular imaging[12-15].

Organic dyes and semiconductor quantum dots (QDs) are two conventional luminescent labeling materials used in bioimaging. However, these materials have intrinsic disadvantages that restrict their application. For example, organic dyes are associated with photobleaching, broad absorption, and emission bands while quantum dots remain controversial due to their inherent toxicity and chemical instability in the body, although they possess good photostability[11, 16, 17]. Recently, rare-earth-based nanoparticles have been proposed as a new generation of biological luminescent labels for their attractive chemical, optical, and biocompatible properties, such as high photochemical stability, long luminescence lifetime (up to several microseconds), low photobleaching, and low toxicity[18-21]. Because of its high quantum efficiency, lanthanide orthophosphate has been widely investigated as a stable luminescence material[22-26]. Liu et al. prepared core-shell structured luminescence nanorods of $LaPO_4:Eu^{3+}@SiO_2$ using hydrothermal and surfactant-free sol-gel methods[27]. Ren et al. fabricated gadolinium orthophosphate ($GdPO_4$) nanorods co-doped with light-emitting lanthanide ions through a hydrothermal method[28]. Zhang et al. introduced a sacrificial-template method for the fabrication of submicrometer-sized $YPO_4:Eu^{3+}$ hierarchical hollow spheres[23]. Di et al. synthesized luminescent $TbPO_4$ and Eu^{3+} doped $TbPO_4$ nanoparticles via a citric-acid-mediated hydrothermal method, and the two types of nanoparticles had a long luminescence lifetime, low cytotoxicity, and high photostability[29]. The doping of Eu^{3+} enhanced the absolute emission quantum yield (QY) of $TbPO_4$ by four times[29]. Nevertheless, investigations of Ce^{3+} doped $TbPO_4$ fluorescent material have rarely been reported.

Gadolinium possesses seven unpaired 4f electrons ($4f^7$), giving it a large electron magnetic moment (S=7/2). As a result, the longitudinal relaxation of water protons can be induced very efficiently by Gd ions. An effective multimodal imaging probe that combines magnetic and optical properties on one particle was achieved by doping Gd^{3+} ions into a light-emitting lanthanide (Ln)-containing host matrix[30-33]. Grzyb et al. used a co-precipitation method to synthesize a multifunctional (luminescent and magnetic) nanomaterial, and observed down- and visible up-conversion of the Yb^{3+} and Tb^{3+} doped $GdPO_4$ nanocrystals[31]. Wang et al. introduced a synthesis for coating a paramagnetic lanthanide complex shell onto rare-earth nanoparticles by chelation for fluorescent and magnetic resonance dual-modality imaging[33]. However, to the best of our knowledge, the synthesis of MR-fluorescence core-shell nanocomposites using a hydrothermal approach has not yet been reported.

In this study, two nanoparticles, $TbPO_4:Ce^{3+}$ and $TbPO_4:Ce^{3+}@TbPO_4:Gd^{3+}$, were successfully synthesized via a citric-acid-mediated hydrothermal route. $TbPO_4:Ce^{3+}@TbPO_4:Gd^{3+}$ has a core–shell structure and was prepared in a second step by using colloidal nanoparticles of $TbPO_4:Ce^{3+}$ as a template. The luminescent and MR contrast properties of the core–shell $TbPO_4:Ce^{3+}@TbPO_4:Gd^{3+}$ nanoparticles (CSNPs) and the cell viability internalized with the CSNPs were systematically characterized. The core-shell nanoparticles reported in this study have the following advantages: (1) suitable size (mean size=58.18nm) for biological applications[34]; (2) good luminescent and fluorescent properties; (3) a high surface to volume ratio for Gd^{3+} ions provided by the $TbPO_4:Gd^{3+}$ nanoshell[35]; and (4) high cell viability for bioimaging and cell labeling applications.

Results and discussion

Structure and morphology characterization

The synthetic procedures are illustrated in Fig. 1. First, hexagonal prism shaped $TbPO_4:Ce^{3+}$ seeds were synthesized via a citric-acid-mediated hydrothermal route, and the $TbPO_4:Gd^{3+}$ nanoshells were then coated using the same process, except a different reactant was used for the gadolinium doping.

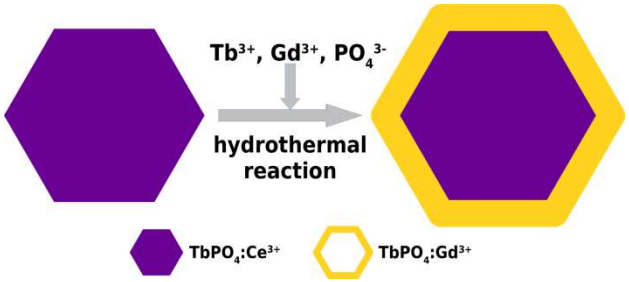

Figure 1. Schematic illustration of the preparation of $TbPO_4:Ce^{3+}@TbPO_4:Gd^{3+}$ by a citric-acid-mediated hydrothermal route.

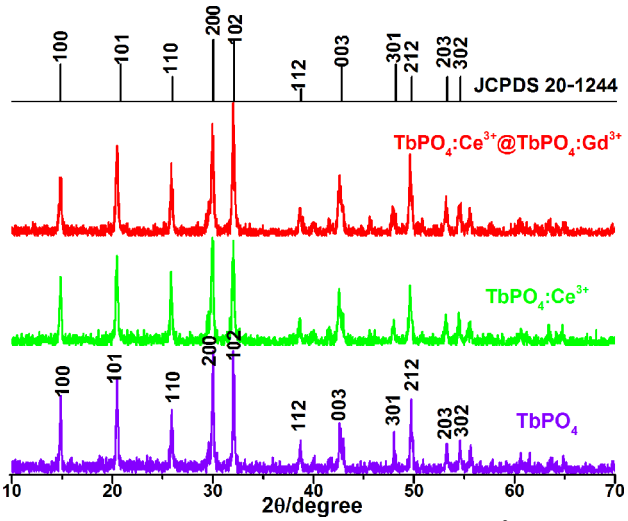

Figure 2. X-ray diffraction patterns of the $TbPO_4:Ce^{3+}@TbPO_4:Gd^{3+}$ nanocrystals by a hydrothermal process. The related patterns for the as-obtained host material, $TbPO_4$, the standard diffraction peaks of hexagonal TbPO4 (JCPDS-20124) and the template material, $TbPO_4:Ce^{3+}$, are also included.

The XRD patterns of the as-synthesized nanocomposites are shown in Fig. 2. Clearly, $TbPO_4$, $TbPO_4:Ce^{3+}$, and $TbPO_4:Ce^{3+}@TbPO_4$: Gd^{3+} can be readily indexed to the pure-phase hexagonal terbium phosphate that corresponds to JCPDS-

201244. All of the as-obtained $LnPO_4$ materials have the same diffraction peaks and good crystallinity without detectable defects. Gd-doping has little effect on the crystalline structure of the matrices, which is easily understood as lanthanide ions have very close atomic radii and similar coordination structures and chemical properties. The change in the crystal structure is insignificant when Tb^{3+} ions are replaced by either Ce^{3+} or Gd^{3+} ions. Fig. 2 shows the main peaks of XRD, (102) and (200), which reveal the existence of certain preferred orientations. The formation of preferred orientations is possibly a result of the citric acid, which acts as chelating agent and induces the sideways growth along directions [102] and [200] in the synthesis process. Similar phenomena have also been observed in the synthesis of other materials[29,36-37]. Compared with pure $TbPO_4$, the peak positions of $TbPO_4$: Ce^{3+} @ $TbPO_4$: Gd^{3+} and $TbPO_4$: Ce^{3+} shift left slightly, and the left shift of $TbPO_4$: Ce^{3+} is larger than that of $TbPO_4$: Ce^{3+} @ $TbPO_4$: Gd^{3+}. This is mainly attributed to the slight difference of Ce, Gd and Tb atomic radius in that R (Tb) < R (Gd) < R (Ce). Judged by the Bragg's law $2dSin\theta=n\lambda$, the diffraction angle 2θ can be easily figured out as follow: the 2θ of $TbPO_4$:Ce^{3+} < the 2θ of $TbPO_4$:Ce^{3+}@$TbPO_4$:Gd^{3+} < the 2θ of $TbPO_4$.

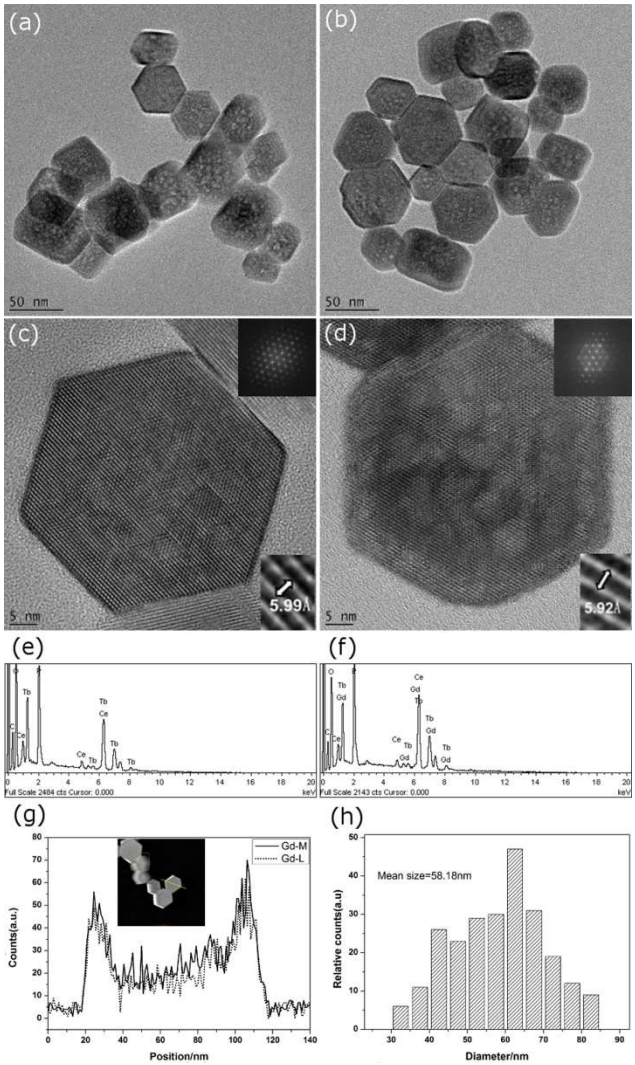

Figure 3. Morphology and structure characterizations. (a) TEM image of $TbPO_4$:Ce^{3+}. (b) TEM image of CSNPs. (c) High-resolution STEM image of $TbPO_4$:Ce^{3+} (right-top inset is the Fourier transform which shows a single crystal structure), the interplanar spacing is 5.99 Å. (d) High-resolution STEM image of CSNPs (right-top inset is the Fourier transform which also shows a single crystal structure), the interplanar spacing is 5.92 Å. (e) EDS spectrum of $TbPO_4$:Ce^{3+}. (f) EDS spectrum of CSNPs. (g) EELS line scan conducted with STEM imaging (inset) of CSNPs. (h) Typical histogram of the size distribution (distance of opposite vertexes) as derived from TEM images (248 particles measured) of the CSNPs.

The size and morphology of the synthesized nanocomposties were characterized using transmission electron microscopy (TEM). Figs. 3a and 3b display TEM images of the template material $TbPO_4$:Ce^{3+} nanoparticles and the CSNPs, respectively. All of the nanoparticles have a similar hexagonal prism shape. Judging by the TEM graphs, the particle sizes of the CSNPs are somewhat larger than those of $TbPO_4$:Ce^{3+}. The high resolution TEM graphs and the corresponding Fourier transforms (insets) in Figs. 3c and 3d show that the nanoparticles are single crystals with a high degree of structural uniformity. The interplanar spacings were calculated as 5.92 Å (Fig. 3c inset) and 5.99 Å (Fig. 3d inset), respectively. It is difficult to discern the shell of the CSNPs from the core by the

TEM image because of their similar crystalline structures. Therefore, EDS and electron energy loss spectroscopy (EELS) were used to scan the profile of the Gd concentrations. Ce was found in both samples (Figs. 3e and 3f) while Gd was only detected in the core-shell sample (Fig. 3f). According to the EELS line scan profile (Fig. 3g), Gd is mainly concentrated on the edge of the nanoparticles, which meets the basic design of the current work to fabricate a nanocomposite with a core-shell architecture and dual imaging functionality (optical modality at the core and MRI modality on the shell). This method was adopted in another study[38]. The sizes of the CSNPs were also measured and counted, and a histogram of the particle size distribution was obtained, which ranges from 40 to 70 nm with an average particle size of 58.18 nm (Fig. 3h). Considered simply in terms of the size and distribution of the particles, the above-mentioned nanoparticles have potential applications in the field of nanomedicine, such as for drug delivery in cancer therapy[34].

Photoluminescence and MRI property characterization

The fluorescent properties of $TbPO_4$:Ce^{3+} and the CSNPs in water-based suspension were tested at room-temperature using the same concentration and instrument conditions. For sake of comparison, undoped $TbPO_4$ was also tested as a reference. The excitation spectra (Fig. 4a, monitoring at 544 nm) indicate that all of the samples have an absorption peak at the 274nm wavelength. The fluorescence intensities of the nanoparticles decline in sequence as CSNPs > $TbPO_4$:Ce^{3+} > $TbPO_4$. The fluorescence intensities of the emission spectra (excited at 274nm) also have a consistent sequence. Four emission peaks can be observed in Fig. 4b, corresponding to the $^5D_4 \rightarrow {}^7F_J$ (J/6, 5, 4, 3) transitions of the Tb^{3+} ions. The most intense peak is located at 544 nm ($^5D_4 \rightarrow {}^7F_5$), which is consistent with the green light observed in the photoluminescence photograph of the CSNPs in the inset of Fig. 4b. Encouragingly, the fluorescence intensities of the CSNPs and $TbPO_4$:Ce^{3+} are greatly enhanced in contrast to undoped $TbPO_4$ by a factor of 200 and 100 times, respectively. In fact, the fluorescence of the nanoparticles is intensified further by the coating of a $TbPO_4$:Gd^{3+} shell. This enhancement can be ascribed to the following three factors:

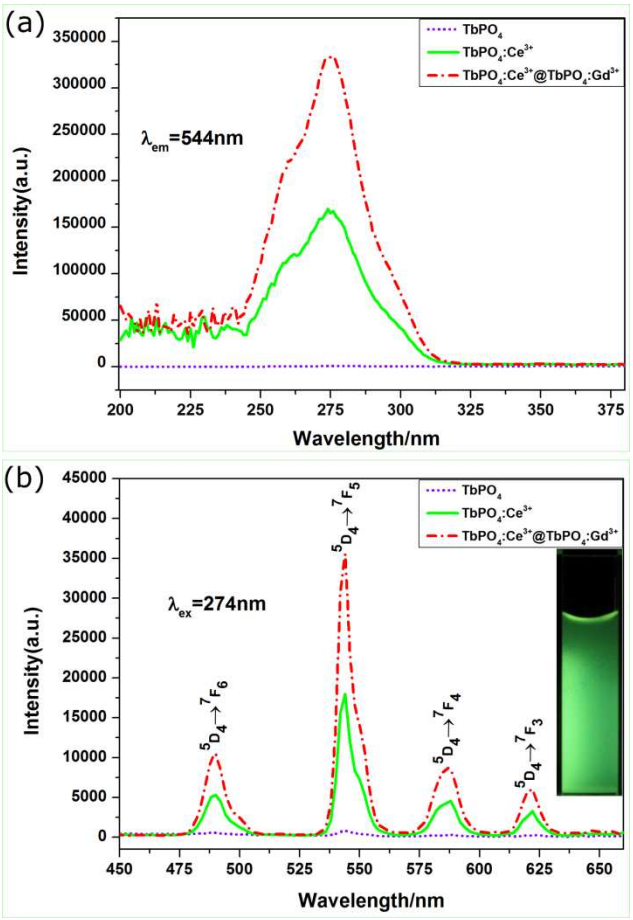

Figure 4. Excitation spectra (a) and emission spectra (b) of the CSNPs, $TbPO_4$, and $TbPO_4$:Ce^{3+}. The inset in (b) is a luminescent photograph of the CSNPs in suspension.

(1) With pure $TbPO_4$, the energy transfer from a Tb^{3+} ion to its defects is more rapid than the transfer to another Tb^{3+} ion nearby[26], which results in energy dissipation and fluorescence quenching. Ce^{3+} doping brings an alternative path of $Ce^{3+} \rightarrow Tb^{3+}$ energy transmission, thus effectively reducing the energy dissipation in the process of energy transfer. The energy gap of $4f^n \rightarrow 4f^{n-1}5d^1$ of Ce^{3+} is narrower than that of Tb^{3+}, therefore $TbPO_4$:Ce^{3+} has stronger absorption under 274 nm exciting light[39-40]. Because the energy state $^2D_{3/2}$ (5d shell) of Ce^{3+} is higher than the $^5D_4$ (4f shell) state of Tb^{3+} [26,41], energy can be effectively transferred from a Ce^{3+} ion to a neighbouring Tb^{3+} ion, thereby increasing the fluorescence intensity. Therefore, the better excitation light absorption, lower energy loss, and more efficient energy transfer jointly contribute to the enhancement of the fluorescence intensity of $TbPO_4$:Ce^{3+} in relation to that of pure $TbPO_4$. (2) $TbPO_4$, $CePO_4$, and $GdPO_4$ share the same crystalline structure, and their lattice parameters are also very close to each other. We thus speculate that the core $TbPO_4$:Ce^{3+} and the shell $TbPO_4$:Gd^{3+} are perfectly joined by a coherent interface. Benefiting from the peculiar microstructure of the core-shell feature, the luminescence of the core is enhanced due to the reduced surface defects, because energy can be easily transferred from Tb^{3+} to the defects[26]. (3) The $TbPO_4$:Gd^{3+} shell located on the surface of the $TbPO_4$:Ce^{3+}

core acts as shield that can significantly reduce the Forster resonance energy transfer, thus effectively inhibiting the fluorescence quenching[42]. As a consequence, the photoluminescent property of the CSNPs is enhanced.

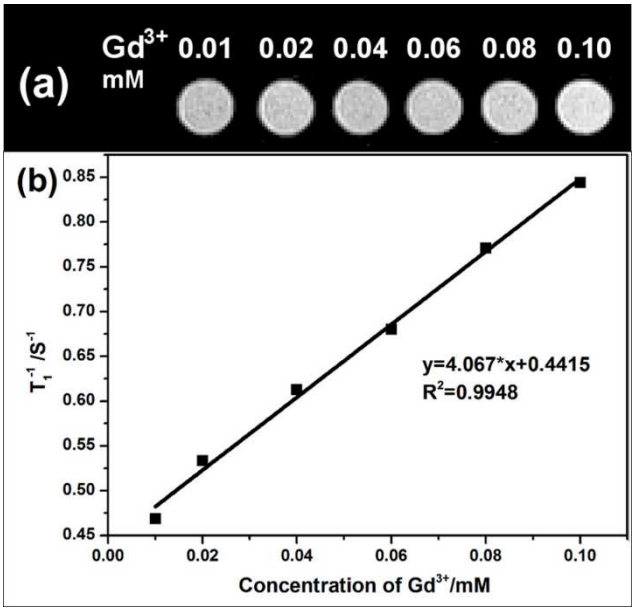

Figure 5. T1-weighted MR imaging of CSNPs dispersed in 0.5wt% agar solution at various Gd^{3+} concentrations (a) and the plot of the relaxation rates (1/T1) versus ion concentrations (b).

The positive signal-enhancement capability of Gd gives Gd-doped materials the potential to act as MR imaging contrast agents. In our work, the CSNPs were appraised for T1-weighted MRI by a 0.55 T MRI instrument (MicroMRI, Shanghai Niumag Corp.). Fig. 5a shows the T1-weighted images of the CSNPs at a series of Gd ion concentrations (0.005, 0.02, 0.05, 0.1, 0.2 mM) identified by inductively coupled plasma atomic emission spectroscopy (ICP-AES) in a solution of 0.5% agar. The MRI signal intensity increases with the Gd ion concentration. The longitudinal relaxation rates (1/T1) were measured and are plotted in Fig. 5b. The longitudinal relaxation rate versus the concentration of Gd ions shows good linearity, and the slope, also known as the longitudinal relaxivity of a MRI contrast agent, equals 4.067 s-1·mM-1. This suggests that the performance of the CSNPs is comparable to that of the commercial MRI contrast agent Gd-DTPA that is widely used in current clinical MRI diagnosis.

Bioimaging property characterization

The biocompatibility of the CSNPs is a vital factor for their possible application in bioimaging and cell labeling, because only biologically nontoxic or biocompatible low-toxic nanomaterials are suitable for biological applications. *In-vitro* cytotoxicity of the CSNPs to HeLa cells was evaluated with methylthiazolyl tetrazolium (MTT) assays. Assuming that the viability of the negative control cells was 100%, less than 15% of the cells died after 48 h incubation at a concentration of 20 μg/ml, as shown in Fig. 6. Even when the concentration was increased to 200 μg/ml, the observed cell viability still remained above 80% after 48 h incubation. Therefore, the CSNPs can be regarded as having low-toxicity even when the $TbPO_4$:Gd^{3+} shell is directly exposed to water. The low toxicity is possibly due to the good crystallinity of the as-prepared CSNPs in that the heavy metal ions Gd^{3+} and Tb^{3+} cannot easily escape from the outside surface of the nanoparticles and dissolve in the surrounding water. This would concur with previous reports that rare-earth-based nanophosphors maintain decent chemical stability and generally low toxicity[18, 28, 29, 32].

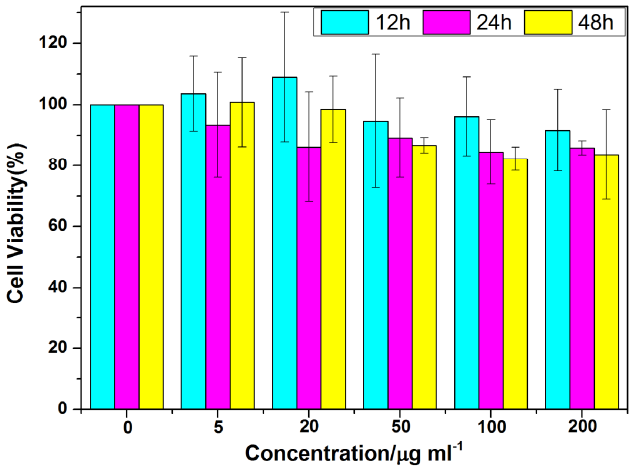

Figure 6. The biocompatibility of the CSNPs analyzed using MTT assays. HeLa cells were incubated with the CSNPs at specific concentrations (0, 5, 20, 50, 100, 200 μg/ml) for 12, 24, and 48 hours at 37℃.

To judge whether the nanocomposites are suitable for luminescent biological labels, we conducted *in-vitro* experiments using HeLa cells. The CSNPs were used in all of the biological experiments because of their high fluorescence quantum yield. The luminescence imaging of the CSNPs in living cells was observed using laser confocal fluorescence microscopy with a 405 nm ultraviolet excitation, and the results are displayed in Fig.7a. Bright intracellular luminescence was detected after cell incubation with 0.5 mg/ml of the CSNPs for 8h at 37℃. As shown in Fig. 7b, there were no evident regions of cell death observed in the bright field image, confirming that the cells were viable throughout the experiments. The superimposition of the confocal fluorescence on the bright-field image in Fig. 7c demonstrates that the CSNPs were internalized by the cells, as the green fluorescence can be clearly observed in the cytoplasm. Due to their excellent cellular internalization and bright intracellular luminescence, the CSNPs show great potential for use in bioimaging and biolabeling.

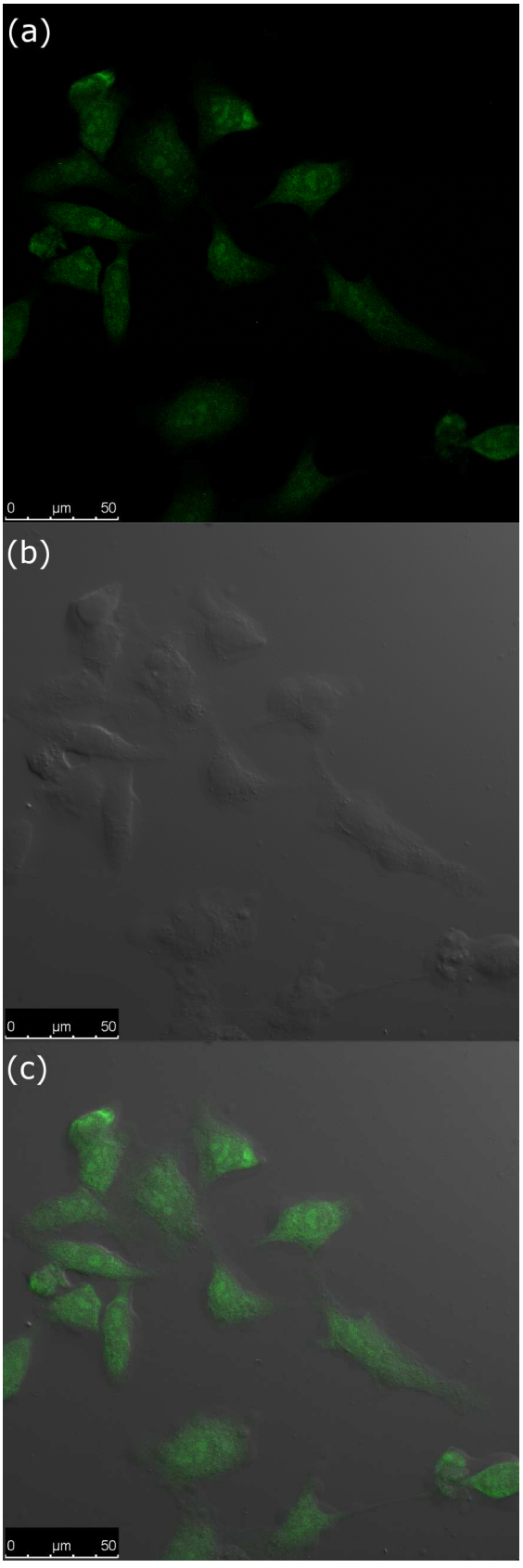

Figure 7. Confocal fluorescence images of HeLa cells after 8 h incubation in 0.5mg/ml CSNPs, using 405 nm irradiation. Fluorescence image (a). Bright-field image of the same zone (b). The fluorescence image is superimposed on the bright-field image (c).

Experimental Section

Materials

$Tb(NO_3)_3 \cdot 6H_2O$ (99.9%) was purchased from Strem Chemicals. $Gd(NO_3)_3 \cdot 6H_2O$ (99.9%) was obtained from Aladdin Chemistry Co. Ltd., $Ce(NO_3)_3 \cdot 6H_2O$ (99%) from Tianjin Kermel Chemical Reagent Co. Ltd., $(NH_4)_2HPO_4$ (99.9%) from Tianjin Rgent Chemical Reagent Co. Ltd., Citric acid (99.5%) from the Tianjin Damao Chemical Reagent Factory, and Ammonia Solution (25%) from the Guangzhou Chemical Reagent Factory. The deionized water and all the other chemicals used in the experiments were analytical grade without further purification.

Rare-earth nitrate ($TbNO_3$,$CeNO_3$ and $GdNO_3$) stock solutions with a metal ion concentration of 0.2M were prepared by dissolving solid powder in deionized water at room temperature.

Synthesis

Synthesis of TbPO4:Ce^{3+}

A 10ml rare-earth nitrate mixture of 0.2 M was prepared by blending $Tb(NO_3)_3$ and $Ce(NO_3)_3$ stock solutions at a volume ratio of 9:1, and then adding 10 ml citric acid aqueous solution (0.4 M) as a ligand. The clear liquid mixture was kept under ultrasonication for 10 minutes, and then vigorously stirred for 10 minutes for intensive mixing. The mixture quickly became turbid after 2.5 mmol $(NH_4)_2HPO_4$ aqueous solution was added. Aqueous ammonia (NH_4OH) was subsequently added drop by drop until the final pH reached 1.5. After additional agitation for 10 min, the mixture was transferred into a 50ml Teflon autoclave, sealed, and heated at 150 ℃ for 20h. Once the autoclave cooled to room temperature, the precipitations were separated by centrifugation and then washed with deionized water and ethanol in turn for three rounds. The $TbPO_4$:Ce^{3+} nanoparticles were attained after being dried in air at 60℃ for 12h.

Synthesis of the CSNPs

The CSNPs were synthesized by using the colloidal nanoparticles of $TbPO_4$:Ce^{3+} (2mmol) as templates. First, the as-prepared $TbPO_4$:Ce^{3+} nanoparticles were dispersed in 10ml deionized water under ultrasonication for 20 minutes. Another liquid precursor was made from stock solutions ($Tb(NO_3)_3$ and $Gd(NO_3)_3$, 0.2M at a volume ratio of 9:1) and citric acid aqueous solution was added to the $TbPO_4$:Ce^{3+} suspension. In this procedure, the same concentration of citric acid (CA) should be maintained. The remaining steps were the same as for the synthesis of $TbPO_4$:Ce^{3+}. The dose of $(NH_4)_2HPO_4$ to be added depends on the total dose of $Tb(NO_3)_3 \cdot 6H_2O$ and $Gd(NO_3)_3 \cdot 6H_2O$, but the concentration of the citric acid ligand should be kept the same as before. If only the total dose of $Tb(NO_3)_3 \cdot 6H_2O$ and $Gd(NO_3)_3 \cdot 6H_2O$ is changed, CSNPs with different core thickness can be obtained. In our synthesis, the Ce^{3+}/Gd^{3+} mole ratio of the CSNPs is 4/1.

Characterization

The crystalline structure of the powder samples was measured by an X-ray diffractometer (D-MAX 2200X VPC,RIGAKU) with Cu-Ka radiation at 30 kV and 30mA, and a 2θ ranging from 10° to 70°. The morphology of the as-synthesised nanoparticles was observed using a transmission electron microscope (TEM, FEI Tecnai- G2 F30) operating at 300 kV. High-resolution STEM images and EELS line scan data were also obtained from the TEM. A histogram of the particle size distribution was constructed by measuring the particles (248 in total) in the TEM images. The chemical composition of the nanoparticles was determined by energy dispersive X-ray spectroscopy (EDS) using an SEM-ED-EBSD instrument and inductively coupled plasma atomic emission spectroscopy (ICP-AES). A combined lifetime and steady state fluorescence spectrometer (FLSP920, Edinburgh Instruments-Ltd) was employed to examine the fluorescence spectra of the nanophosphors.

In-vitro MR imaging

Several 1 ml suspension liquids of the CSNPs with various Gd ion concentrations were first prepared by dispersing the CSNPs powders in deionized water. The solution was then transferred to a series of 1.5 mL tubes. After adding 0.2ml 3% agarose gel into each tube, samples with various Gd iron concentrations (0, 0.01 0.02, 0.04, 0.06, 0.08, 0.1mM) were prepared for the MR relaxivity and MR imaging experiments. The T1 relaxation time of the CSNPs at different concentrations was measured by a 0.55T MRI scanner (PQ001, Shanghai Niumag Electronic Technology Co. Ltd.). The following parameters were adopted for the measurements: P90(us)=13.00, P180(us)=26.00, TD=961720, SW(KHz)=200, TR(ms)=15000, RG1=20, RG2=3, NEX=2, D1(ms)=1950, sampling number=36, and temperature=32℃. The r1 values were calculated through the linear fitting of the 1/T1 relaxation time (s^{-1}) versus the Gd concentration (mM), with the slope of the line describing the longitudinal relaxivity. The MR imaging was performed with a 0.55 T MR imaging instrument (MiniMR-60, Shanghai Niumag Electronic Technology Co. Ltd.). The measurement conditions were as follows: FOV Read=100mm, FOV Phase=100mm, number of excitations (NEX)=4, repetition time (TR)=800ms, echo time (TE)=18.2 ms, slice thickness=5mm, and temperature=32℃.

In vitro confocal microscopy imaging

HeLa cells (logarithmic growth phase, 3.84×10^6/L) were plated on 10mm glass cover slips and allowed to adhere in 500μl 10% fetal bovine serum (FBS) Dulbecco's modified Eagle's medium (DMEM) for 24h at 37℃ under 5% CO_2. After washing with phosphate buffer solution (PBS), the cells were incubated in a culture media containing 500μg/ml $TbPO_4:Ce^{3+}@TbPO_4:Gd^{3+}$ for another 8h at 37℃ under 5% CO_2, and then washed with PBS to remove excess nanoparticles. The down-conversion fluorescence imaging was performed using a laser scanning confocal microscope (TCS SP8, LEICA) operating at an excitation wavelength of 405 nm.

In vitro cytotoxicity

The *in vitro* cytotoxicity of the core-shell $TbPO_4:Ce^{3+}@TbPO_4:Gd^{3+}$ nanoparticles (CSNPs) was measured using a methylthiazolyl tetrazolium (MTT) colorimetric assay. Five thousand HeLa cells (logarithmic growth phase, 5×10^7/L) were seeded in the wells of 96-well plates and grown at 37℃ under 5% CO_2. After 24 h growth, the culture medium was replaced with a fresh medium containing varying concentrations of CSNPs (5, 20, 50, 100, 200 μg/ml). After further cultivation for varying amounts of time (12, 24, 48h), 10 μL MTT dye solution was added to each well. After another 4 h of incubation at 37℃ under 5% CO_2, the medium was removed carefully, and 200 uL dimethyl sulfoxide (DMSO) solution was added to dissolve the formazan crystals for 20 minutes. The absorbance of each well was determined by a microplate reader (M200, TECAN) at 570 nm. The relative cell viability (%) in the control wells containing the cell culture medium without nanoparticles was calculated by [A]test/[A]control×100. Each measurement was repeated at least three times to obtain the mean cell viability and the standard deviation.

Conclusions

A typical two-step hydrothermal synthesis method was used to prepare $TbPO_4:Ce^{3+}@TbPO_4:Gd^{3+}$, which is a new nanocomposite with a core-shell framework and dual-modality of fluorescence and magnetic resonance. The as-synthesized $TbPO_4:Ce^{3+}$ @ $TbPO_4$: Gd^{3+} nanocomposites are hexagonal prisms ranging from 40 to 70 nm in size (58.18 nm on average) and with good crystallinity in terms of X-ray diffraction. The excitation and emission spectra show that the fluorescence of the nanoparticles is increased by 200 times compared to undoped $TbPO_4$. The intracellular fluorescence imaging of the nanoparticles demonstrates their functionality as a biomarker for living cells. The longitudinal relaxivity of the Gd-doped nanoparticles for MRI is $4.067s^{-1}M^{-1}$, which is comparable to that of the commercial MRI contrast agent Gd-DTPA ($4.167s^{-1}M^{-1}$). The *in-vitro* cytotoxicity tests based on the MTT assay demonstrate that the monodispersed core-shell structure $TbPO_4:Ce^{3+}@TbPO_4:Gd^{3+}$ nanocomposites have low cytotoxicity. In conclusion, the $TbPO_4:Ce^{3+}@TbPO_4:Gd^{3+}$ nanocomposites synthesized in this work combine the advantages of good crystallinity, high quantum yield rates, considerable longitudinal relaxivity, and low toxicity, and have good potential to serve as bifunctional contrast media in biomedical diagnosis and analysis.

Acknowledgements

This study was supported by the National Natural Science Foundation of China (Grant No. 11274394), the Natural Science Foundation of Guangdong Province (Grant No. S2012010010542), the Fundamental Research Funds for the Central Universities (Grant No. 11lgjc12), and the Specialized

Research Fund for the Doctoral Program of Higher Education (Grant No. 20110171110023).

Notes and references

1. L. Y. Zeng, L. C. Xiang, W. Z. Ren, J. J. Zheng,T. H. Li,B. Chen, J. C. Zhang, C. W. Mao,A. G. Li and A.G. Wu, RSC Adv., 2013, 3, 13915–13925.
2. J. Yu, R. Hao, F.G. Sheng, L. L. Xu, G. J. Li and Y. L. Hou, Nano Res., 2012, 5, 679–694.
3. A. Xia, Y. Gao, J. Zhou, C. Y. Li, T. S. Yang, D. M. Wu, L. M. Wu and F. Y. Li, Biomaterials, 2011, 32 ,7200–7208.
4. C. Y. Liu, Z. Y. Gao, J. F. Zeng, Y. Hou, F. Fang, Y. L. Li, R.R. Qiao, L. Shen, H. Lei, W. S. Yang and M. Y. Gao, ACSNANO, 2013, 7, 7227–7240.
5. Y. Yang, Y. Sun, T. Y. Cao, J. J. Peng, Y. Liu, Y. Q. Wu, W. Feng, Y. J. Zhang and F. Y. Li, Biomaterials, 2013, 34,774–783.
6. J. Cheon and J. Lee, Accounts of Chemical Research, 2008, 41, 1630–1640.
7. D. T. Tu, Y. S.Liu, H. M. Zhu and X. Y. Chen, Chem. Eur. J, 2013, 19, 5516–5527.
8. H. Zhu , Y. L. Shang , W. H. Wang , Y. J. Zhou , P. H. Li , K. Yan , S. L. Wu , K. Yeung , Z. S. Xu , H. B. Xu and P. Chu, Small, 2013, 9, 2991–3000.
9. N. Nuñez, S. Rivera, D. Alcantara, J. Fuente, J.Sevillano and M. Ocaña, Dalton Trans., 2013, 42, 10725–10734.
10. X. J. Zhu, J. Zhou, M. Chen, M. Shi, W. Feng and F. Y. Li, Biomaterials, 2012, 33, 4618–4627.
11. J. Zhou, X.J. Zhu, M. Chen, Y. Sun and F. Y. Li, Biomaterials, 2012, 33, 6201–6210.
12. J. Zhou, Z. G. Lu, G. G. Shan, S. H. Wang and Y. Liao, Biomaterials, 2014, 35, 368–377.
13. L. Q. Xiong, Z. G. Chen, M. X. Yu, F. Y. Li, C. Liu and C. H. Huang, Biomaterials, 2009, 30 5592–5600.
14. J. Zhou, Y. Sun, X. X. Du, L. Q. Xiong , H. Hu and F. Y. Li, Biomaterials, 2010, 31, 3287–3295.
15. C. Wang, L. Cheng and Z. Liu, Biomaterials, 2011, 32, 1110–1120.
16. R. R. Qiao, J. F. Zeng, Q. J. Jia, J. Du, L. Shen, Acta Phys. Chim. Sin., 2012, 28, 993–1011.
17. J. Shen, L. D. Sun, Y. W. Zhang and C. H. Yan, Chem. Commun, 2010, 46, 5731–5733.
18. Fen Zhang and S. Wong, ACSNANO, 2010, 4, 99–112.
19. C. Granadeiro, B. Castro, S. Balula and L. Silva, Polyhedron, 2013, 52, 10–24.
20. S. Eliseeva and J. Bünzli, Chem. Soc. Rev., 2010, 39, 189–227.
21. L. Yang, L. Q. Zhou, X. Chen, X. L. Liu, P. Hua, Y. Shi, X. G. Yue, Z. W. Tang and Y. Huang, Journal of Alloys and Compounds, 2011, 509, 3866–3871.
22. W. Wang, X. P Jiang and K. Z. Chen, Chem. Commun., 2012, 48, 6839–6841.
23. L. H Zhang, G. Jia, H. P. You, K. Liu, M. Yang, Y. H. Song, Y. H. Zheng, Y. J. Huang, N. Guo and H. J. Zhang, Inorganic Chemistry, 2010, 49, 3305–3309.
24. H. Y. Bai, G. X. Liu, X. X. Dong and J. X. Wang, Acta Chimica Sinica, 2011, 69, 783-788.
25. J. T. Lü, T. Fan, J. N. Xie and G. J. Chen, Optics Communications, 2013, 286, 221–223.
26. Y. Ruan, Q. B. Xiao, W. Q. Luo, R. F. Li and X. Y. Chen, Nanotechnology, 2011, 22, 275701.
27. G. X. Liu, N. L. Li, X. T. Dong and J. X. Wang, Chinese Journal Of Luminescence, 2011, 32, 466–470.
28. W. L. Ren, G. Tian, L. J. Zhou, W. Y. Yin, L. Yan, S. Jin, Y. Zu, S. J. Li, Z. J. Gu and Y. L. Zhao, Nanoscale, 2012, 4, 3754–3760.
29. W. H. Di, J. Li, N. Shirahata, Y. Sakka, M. Willingere and N. Pinna, Nanoscale, 2011, 3, 1263–1269.
30. B. Abécassis, F. Lerouge, F. Bouquet, S. Kachbi, M. Monteil, and P. Davidson, J. Phys. Chem. B,2012, 116, 7590−7595.
31. T. Grzyb, A. Gruszeczka, R. Wiglusz, Z. Sniadecki, B. Idzikowski and Stefan Lis, J. Mater. Chem., 2012, 22, 22989–22997.
32. S. Liviano, A. Becerro, D. Alcántara, V. Grazú , J. Fuente and M. Ocaña, Inorg. Chem., 2013, 52, 647−654.
33. Y. Wang, L. Ji, B. B. Zhang, P. H. Yin, Y. Y. Qiu, D. Q. Song, J. Y. Zhou and Q. Li, Nanotechnology, 2013, 24, 175101.
34. K. Bourzac, Nature, 2012, 491, 58-60.
35. H. Liu, L. Li, X. M. Tian, W. Y. Hu, X. Y. Kuang, and Y. Z. Shao, Eur. J. Inorg. Chem., 2012, 5677–5684.
36. L. Yang, L. Q Zhou, X. G. Chen, X. L. Liu, P. Hua, Y. Shi, X. G. Yue, Z. W. Tang, Y. Huang, Journal of Alloys and Compounds, 2011,509, 3866–3871.
37. L. Xu, C. L. Lu, Z. H. Zhang, X. Y. Yang and W. H. Hou, Nanoscale, 2010, 2, 995–1005.
38. F. Wang, R. R. Deng, J. Wang, Q. X. Wang, Y. Han, H. M. Zhu, X. Y. Chen and X. G. Liu, Nature Materials, 2011, 10, 968-973.
39. S. V. Eliseeva and J. C. G. Bunzli. Chemical Society Reviews, 2010, 39, 189-227.
40. P. Hanninen and H. Harma. Lanthanide Luminescence: Photophysical, Analytical and Biological Aspects. Springer-Verlag, Berlin, 2011. p. 14.
41. J. R. Bao, X. W. Zhu, S. X. Jin, Y. Lv, L. C. Xiong, C. F. Li and W. X. Li, Spectroscopy and Spectral Analysis, 2013, 33, 27–30.
42. Y. Y. Fan, Z. C. Hua, J. Yang, C. Zhang and L. Zhu, Applied Surface Science, 2013, 266, 22–26.

